Cryo-EM structure of the *Plasmodium falciparum* 80S ribosome bound to the anti-protozoan drug emetine

Wilson Wong[1,2*], Xiao-Chen Bai[3*], Alan Brown[3*], Israel S. Fernandez[3], Eric Hanssen[5], Melanie Condron[1,2], Yan Hong Tan[1,2], Jake Baum[1,2,4#] and Sjors H. W. Scheres[3#]

[1] Division of Infection and Immunity, Walter and Eliza Hall Institute of Medical Research, Parkville, Victoria, 3052, Australia.

[2] Department of Medical Biology, University of Melbourne, Parkville, Victoria, 3010, Australia.

[3] MRC Laboratory of Molecular Biology, Cambridge Biomedical Campus, Cambridge CB2 0QH, UK.

[4] Department of Life Sciences, Imperial College London, South Kensington, London, SW7 2AZ, UK.

[5] Electron Microscopy Unit, Bio21 Molecular Science and Biotechnology Institute, University of Melbourne, Parkville, Victoria 3010, Australia.

*These authors contributed equally to this work.

Abstract

Malaria inflicts an enormous burden on global human health. The emergence of parasite resistance to front-line drugs has prompted a renewed focus on the repositioning of clinically approved drugs as potential anti-malarial therapies. Antibiotics that inhibit protein translation are promising candidates for repositioning. We have solved the cryo-EM structure of the cytoplasmic ribosome from the human malaria parasite, *Plasmodium falciparum*, in complex with emetine at 3.2 Å resolution. Emetine is an anti-protozoan drug used in the treatment of amoebiasis that also displays potent anti-malarial activity. Emetine interacts with the E-site of the ribosomal small subunit and shares a similar binding site with the antibiotic pactamycin, thereby delivering its therapeutic effect by blocking mRNA/tRNA translocation. As the first cryo-EM structure that visualizes an antibiotic bound to any ribosome at atomic resolution, this establishes cryo-EM as a powerful tool for screening and guiding the design of drugs that target the parasite translation machinery.

Introduction

Malaria is responsible for an estimated 627,000 annual deaths worldwide, with the majority of victims being children under five years of age (1). At present there is no licensed malaria vaccine and parasites have developed resistance to all front-line anti-malarial drugs. As such, there is an urgent need for novel therapeutics that can be used as monotherapies or as partner drugs for combinatorial regimes (2). An alternative to novel candidates is the repurposing or repositioning of clinically approved drugs that can be used in combination with known anti-malarials, such as chloroquine, antifolates and artemisinin, to increase their useable lifespan by reducing resistance (3).

The etiological agents for malaria are a family of unicellular protozoan pathogens of the genus *Plasmodium*. The parasite has a complex two-host lifecycle with a sexual stage occurring in the mosquito vector and an asexual stage in the human host. It is during the asexual blood stage that disease symptoms in humans first appear, including those associated with severe malaria, and it is often at this stage that the need for clinical intervention becomes apparent (4). Much of malaria pathology is the result of exponential growth of the parasite within erythrocytes, and given the critical role that protein synthesis plays in this, the translational machinery is an attractive drug target.

Protein translation in the parasite is focused on three centers (5): the cytoplasmic ribosome, responsible for the vast majority of protein synthesis, and organellar ribosomes of the mitochondrion and non-photosynthetic plastid, termed the apicoplast (6). In addition, and unusually for a eukaryotic cell, *Plasmodium* species have two distinct types of cytoplasmic ribosome that differ in their ribosomal RNA (rRNA) composition. These are expressed at different stages of the lifecycle, one predominantly in the mosquito vector and the other in the mammalian host, with evidence that both can occur simultaneously for limited periods (7).

Antibiotics known to target the apicoplast ribosome, such as the macrolide azithromycin, demonstrate a delayed-death effect, whereby treated parasites die in the second generation of drug exposure, and therefore have slow clinical onset (8, 9). However, because anti-malarial treatment at the blood-stage requires rapid intervention, we focused on the dominant, blood stage-specific cytoplasmic ribosome from the most virulent form of *Plasmodium, P. falciparum* (*Pf*80S) (7), as inhibition of cytosolic translation would be expected to be direct and fast-acting. *Pf*80S is both a candidate for development of novel

therapeutics that target specific differences between itself and its counterpart in the human cytosol, and also for repurposing of anti-protozoan inhibitors, such as emetine (10).

In this present study, we solved the structure of *Pf*80S-emetine complex at 3.2 Å resolution and built a fully-refined all-atom model. This represents, to our knowledge, the first structure of an entire eukaryotic ribosome at atomic resolution solved by electron cryo-microscopy (cryo-EM). *Pf*80S has a broad distribution of *Pf*-specific elements across its surface, with particularly long rRNA expansion segments (ESs) in the small subunit. The atomic structure of *Pf*80S in complex with emetine reveals the molecular basis of this clinically relevant anti-protozoan translation inhibitor. In doing so, we establish cryo-EM as a powerful tool for structure-based drug design.

Results

Cytoplasmic ribosomes were isolated from the 3D7 strain of *P. falciparum* parasites maintained in human erythrocytes (Figure 1A, B). Limitations in parasite culture volume, yielding ~10^{10} parasitized red blood cells and low yield of sample material (1g of parasites yielded 0.35 mg *Pf*80S), precluded an ability to crystallize *Pf*80S to solve the structure by conventional X-ray crystallography. We therefore exploited recent advances in direct electron detection and statistical image processing (11) (12) to determine the structure by cryo-EM at an overall resolution of 3.2 Å (Figure. 1C-E and figure supplement 1).

Protein side chains and RNA bases were clearly resolved in our maps (Figure 1D). The use of model building and refinement tools that were adapted from X-ray crystallography (13) led to a near-complete atomic model with excellent geometrical properties (Figure 2A,B and Table 1). The ribosome model comprises the large (*Pf*60S) and small subunit (*Pf*40S) with a total of 74 proteins (Table 2 and 3) as well as the 5S, 5.8S, 18S and 28S rRNAs and a tRNA bound at the E-site. The head region of *Pf*40S has weaker density than the rest of the ribosome due to the inherent flexibility at the neck (centered around h28). This meant that eS31, located in the beak of the 40S head (14), could not be positioned accurately, and has therefore been omitted from the final model. Using base-pair information extracted directly from the atomic model it was possible to revise secondary structure diagrams for *P. falciparum* rRNA (Figure 2-figure supplement 1-3), facilitating comparison with rRNA of other species.

Currently, high resolution structures of eukaryotic ribosomes have been solved using X-ray crystallography and are limited to just three structures; the individual subunits from a ciliated

protozoan, *Tetrahymena thermophila* (14, 15), and the complete 80S ribosome from the yeast *Saccharomyces cerevisiae* (16). These models have been used to interpret lower resolution structures solved by cryo-EM of other species including the yeast *Kluyveromyces lactis* (17), *Drosophila melanogaster* (18), *Trypanosoma brucei* (19) as well as human ribosomes (18) and provide the basis of the nomenclature used for describing the structures.

To examine overall architectural differences we compared the model of *Pf*80S to yeast 80S (16). Perhaps the largest difference is the absence of RACK1 (Figure 1A and B), which associates with the head of the 40S in the vicinity of the mRNA exit channel (14, 20) and has been identified in all eukaryotic ribosome structures solved to-date. RACK1 serves as a signaling scaffold that can recruit other proteins to the ribosome and may link the ribosome with signal transduction pathways, thus allowing translation regulation in response to stimuli. It has also been proposed that RACK1 promotes the docking of ribosomes at sites where local translation is required (21).

*Pf*RACK1 is conserved with its human homolog with an identity of 60%. The binding site on the ribosome, which comprises eS17, uS3 and 18S rRNA helices h39 and h40 (Figure 1A and B), also appears highly conserved (14). However, the C-terminus of uS3 is not resolved in our structure and probably only becomes ordered upon binding RACK1. The absence of *Pf*RACK1 as an integral member of the small subunit indicates either a different mode of interaction between the ribosome and *Pf*RACK1 in *Plasmodium* compared to humans, or that under the culturing conditions used *Pf*RACK1 is not expressed, or expressed in a form that does not interact with the ribosome. In yeast, RACK1 has been shown to be present in both a ribosome- and a non-ribosome-bound form dependent on growth conditions (22). If the interaction between *Pf*RACK1 and the *Pf*40S is weaker than in other organisms, the possibility that *Pf*RACK1 dissociated during purification and grid preparation cannot be discounted.

The yeast 80S structure was also solved in the presence of STM1, a translation repressor protein, that binds to the head region of the 40S and blocks mRNA entry and binding of tRNA to the A- and P-sites (14). The human and *D. melanogaster* structures also co-purified with an STM1-like protein (SERBP1 and VIG2 respectively) (18). *Pf*80S is not bound by a suppressor molecule, as also observed for the *T. brucei* structure (19), and hence reflects a ribosome capable of active translation.

143 *Pf*80S co-purifies with a tRNA bound to the E-site. Although the density is not well resolved,
144 presumably as a result of low and mixed occupancy, it could be interpreted by positioning a
145 model of $tRNA^{Met}$. The presence of tRNA helps to partially stabilise the L1 stalk near the
146 elbow of the tRNA, however the stalk remains considerably flexible and is averaged out of
147 the high-resolution reconstruction.
148
149 Perhaps due to the absence of RACK1 and/or STM1 or the presence of an E-site tRNA the
150 head of *Pf*40S adopts an orientation with respect to the body that is different to the yeast
151 structure, with uS11 at the beak of the small subunit displaced by more than 10 Å. The root
152 mean square deviation (RMSD) of the two small subunits is 2.9 $Å^2$, however if the head and
153 body are superimposed independently this improves to 1.0 $Å^2$ and 1.5 $Å^2$ respectively. The
154 structure of *Pf*60S superimposes with the yeast 60S with a RMSD of 1.6 $Å^2$. The largest
155 morphological differences in this subunit result from a cluster of rRNA helices (ES7AL,
156 ES15L, and ES7CL) protruding at the solvent side.
157
158 Given the potential of *Pf*80S as a drug target, we sought to describe its detailed structure in
159 comparison to its direct counterpart in the human cytoplasm, where a 4.8 Å cryo-EM 80S
160 structure represents the highest resolution solved to-date (18). Therefore, all protein
161 extensions and rRNA expansion segments (ESs) are annotated on the basis of comparison
162 with human ribosomes. While the core of the *Pf*80S and human ribosome are conserved, the
163 periphery of the ribosomes differs extensively in the nature and length of rRNA ESs and
164 protein extensions. The constraints on rRNA expansion appear to be fewer than on protein
165 extension, as rRNA contributes greater to the mass difference between species.
166
167 Compared to human ribosomes, *P. falciparum* typically has shorter ESs, some of which are
168 entirely absent in the large subunit (ES7D-HL, ES9AL, ES10L, ES20L, ES30L)(Table 4). The
169 functions, if any, of many of these ESs are not well known. ES7E, which is highly conserved
170 in vertebrates, is implicated in selenoprotein synthesis by binding the SBP2 protein that
171 specifically recruits the selenocysteine-specific tRNA and elongation factor (23). While *P.*
172 *falciparum* does utilize selenocysteine, it is incorporated into very few proteins (24) and there
173 is no homolog of SBP2, providing a possible explanation for why ES7E is not present in
174 *Plasmodium*.
175
176 The largest *Pf*-specific ESs are concentrated in the 18S rRNA, with ES6S and ES9S being
177 particularly extended (Figure 2C-D; Figure 2-figure supplement 1). These ESs, like those
178 described in both the human (18) and *Trypanosoma brucei* (19) ribosome structures, are
179 highly flexible and, in our structure, are only partly visible using a map filtered at 6 Å (Figure

2C,D). We have therefore not included these sections in our atomic model. ES10S is located at the top of the 40S head and has been partially built.

P. falciparum ribosomes resemble those of *T. brucei* in that both have large ES6S and ES7S, although these are slightly larger in *T. brucei* (19). ES6S is in contact with ribosomal components that form part of the mRNA entry and exit sites and was therefore suggested as being involved in translation initiation (25). Recently, ES6/7S have been implicated in binding of the conserved translation initiation factor eIF3 based on superposition with a mammalian 43S complex (26). Almost 90 nucleotides of ES6AS are averaged out of our high-resolution reconstruction indicating this stalk is highly flexible, perhaps acting in a manner similar to the P stalk (known as the L7/L12 stalk in prokaryotes) by recruiting factors necessary for translation (in this case eIF3). The other large ES of the 18S rRNA, ES9S, is positioned at the head of the 40S. Given both the intrinsic mobility of the head and presumably the ES itself, there is no density for this ~150 nucleotide *Pf*-specific element and the role it plays remains unclear.

The sites of *Pf*-specific elements are broadly distributed across the solvent-accessible surface of the ribosome, although the region surrounding the exit tunnel is conserved (15) and undecorated with ESs and protein extensions (Figure 2C,D). The subunit interface and eukaryotic-specific bridges, which in addition to having structural roles help transmit information to coordinate activity during translation (16), are generally highly conserved in *Pf*80S. There are a couple of examples of stabilizing interactions that are not observed in human ribosomes. Firstly, eL41, the smallest ribosomal protein, bridges the two subunits (16) and has a 14-residue *Pf*-specific N-terminal extension that reaches into a pocket formed by 18S rRNA of the small subunit and tightly anchors the protein (Figure 3A). Secondly, an additional small bridge (~200 $Å^2$) is formed between the platform of *Pf*40S and the region around the L1 stalk by the C-terminal helix extension of eL8 interacting with the C-terminal helix of eS1 (Figure 3B).

Further ordered *Pf*-specific elements are concentrated near the L1 and P stalks of *Pf*60S. Directly above the P stalk, the *Pf*-specific ES7B1L forms a diverted part of ES7CL that is stabilized by several electrostatic interactions with a C-terminal helix extension of uL4 (Figure 3C). Towards the back of the P-stalk, the C-terminal helix extension of eL14 caps the stem loop of ES7BL (Figure 3C). On the opposite side of the ribosome, near the E-site tRNA, the *Pf*-specific stem loop ES34L is positioned directly above the L1 stalk (Figure 3D). This ES appears to have caused a 60° rotation of the C-terminal helix of eL13 relative to its position in human ribosomes (Figure 3D). The tip of the helix is displaced by ~28 Å away

from the L1 stalk and now stabilizes the interaction between ES34L and the loop of h22. Since the L1 stalk is required for coordinating the movement of tRNAs and the P stalk is required for coordinating the movement of translation factors during the various steps of protein synthesis (27), the expanded mass around the stalks of *Pf*80S may have functional implications for translation in *P. falciparum*.

The ability to determine atomic-resolution structures of *Pf*80S provides a platform for investigating the action of anti-malarial therapeutics that target the ribosome. The clinically used, broad-spectrum eukaryotic translation inhibitor emetine (Figure 4A) (28), has been reported to act as a translocation inhibitor targeting the ribosome (29, 30), although its precise mode of action is unknown. Emetine is a natural product alkaloid from the plant *Carapichea ipecacuanha*, and an approved medicine for the treatment of amoebiasis (31). Although its toxicity associated with chronic usage in humans has limited its clinical use against malaria in its current formulation (32), emetine does demonstrate potent antimalarial activity with a 50% inhibitory concentration (IC_{50}) of 47 nM against the blood stage of multidrug resistant strains of *P. falciparum* (10). Moreover, the immediate therapeutic effect it offers by rapid killing of blood stage parasites may warrant re-consideration of the use of emetine or its derivatives for short periods during acute malaria infection (33).

Incubation of purified *Pf*80S with a 1 mM emetine solution prior to cryo-EM grid preparation, led to a 3.2 Å resolution structure of the complex. Using soft masking, the resolution for the large subunit improved to 3.1 Å, with the small subunit at 3.3 Å (Figure 1C). A difference map was calculated from the reconstructions with and without emetine and showed a single, continuous feature near the E-site of *Pf*40S with a shape and size congruent with a single emetine molecule when thresholded at five standard deviations, and with a maximum value of 11 standard deviations (Figure 4B). At this position in our map the density provided sufficient detail to confidently model the emetine molecule (Figure 4C-E). The emetine binding pocket is formed at the interface between 18S rRNA helices 23, 24, 45 and the C-terminus of uS11 (Figure 5A). Comparison with the unliganded map showed that binding of emetine does not induce changes to the pocket (Figure 4C-D). The benzo[a]quinolizine ring of emetine mimics a base-stacking interaction with G973 of h23 and its ethyl group forms a hydrophobic interaction with C1075 and C1076 of h24, whereas the isoquinoline ring is stacked against the C-terminal Leu151 of uS11 (Figure 5B,C). The interaction is stabilized by a hydrogen bond formed between the NH group of the isoquinoline ring in emetine and an oxygen atom on the backbone of U2061 of h45 (Figure 5B,C). Although there is no high-resolution structure of the human cytoplasmic ribosome, comparison of the emetine binding site in *Pf*80S with the equivalent region in the 4.8 Å human structure (18) revealed that each

of the core binding elements are conserved (Figure 5-figure supplement 1) indicating that emetine likely binds to the cytoplasmic host ribosomes in the same way, potentially accounting for the observed cytotoxicity in humans.

The identified binding site is consistent with mutations of Arg149 and Arg150 of uS11 in Chinese hamster ovary (CHO) cells that have been found to confer resistance to emetine (34). At the emetine-binding pocket, h24 is sandwiched between the apexes of h23 and h45. The C-terminus of uS11 adopts a long coil with seven basic residues (residues 141-151; RKKSGRRGRRL), which form electrostatic interactions with the phosphate backbones of h45, h23 and h24, thereby stabilizing the conformation of this coil together with the 18S rRNA (Figure 5A). This would explain the molecular basis for resistance whereby mutations of the C-terminal arginine residues of uS11 destabilize h23 and h45, disrupting the binding pocket.

The mode of binding of emetine resembles the way in which pactamycin, previously thought to be a unique class of antibiotic, binds to the bacterial 30S (35). In both structures the guanine base at the tip of h23 (G973 in *Pf*; G693 in bacteria) forms a stacking interaction with the hydrophobic rings of either compound. Moreover, the two cytosine bases of h24 (C1075 and 1076 in *Pf;* C795 and 796 in bacteria) are each involved in drug binding (35) (Figure 6). The hydrogen bond to the backbone of h45 and the hydrophobic interaction with Leu151 of uS11 are specific to the *Pf*80S-emetine interaction. In the 30S-pactamycin complex, the last base of the E-site codon of the mRNA was displaced 12.5 Å compared to the native path of mRNA (35) thereby blocking mRNA/tRNA entry into the E-site during the translocation step of protein synthesis (29). Based on these structures, emetine appears to elicit its inhibitory effect by the same mechanism as pactamycin.

Discussion

The resolution revolution in cryo-EM (36) is the product of a new generation of sensors that detect electrons directly (without first converting to light) and have improved quantum efficiencies. These cameras are fast enough to follow beam-induced movement of the particles caused by irradiation with electrons. Statistical movie processing can compensate for this movement allowing for structures to be solved at atomic precision. We have harnessed these technological advances to determine the first structure of a ribosome from a parasite at atomic resolution. Previously, structures of eukaryotic cytosolic 80S ribosomes at a similar resolution had only been possible using X-ray crystallography (16). From the

reconstruction of *Pf*80S-emetine complex at 3.2 Å, we determined a stereochemically accurate all-atom model using recent developments in model building, refinement and validation (13).

The structure of *Pf*80S further demonstrates the diversity of ribosome structures among eukaryotes, especially in terms of the location and nature of ESs at the periphery, while maintaining a conserved core. The observation of *Pf*-specific features could serve as the basis for exploring their functional relevance as an essential, first step towards finding efficacious and clinically safe anti-malarial drugs. An alternative to drug development against *Pf*-specific ribosomal elements is the repurposing of existing antibiotics as anti-malarials. By determining the structure of *Pf*80S in both a liganded and unliganded state we were able to locate the binding site of the anti-protozoan inhibitor, emetine, using an unbiased difference map. That emetine and pactamycin share a binding pocket in eukaryotic ribosomes could not be predicted based on the chemical structures of the drug molecules only. Pactamycin itself has been shown to have potent antiprotozoal activity against both drug-susceptible and drug-resistant strains of *P. falciparum* (37). Chemical modifications to pactamycin have yielded analogs that maintain antimalarial activity but with reduced cytotoxicity against mammalian cells (38). Similarly, an emetine derivative, dehydroemetine, which differs by the presence of a double bond next to the ethyl group of benzo[a]quinolizine ring, exhibits less toxic effects than the parental compound while maintaining anti-parasitic properties (32, 39). This suggests that compounds targeting the emetine/pactamycin binding site are amenable to optimization, potentially leading to drugs more suited to clinical use. The *Pf*80S-emetine structure reveals an edge centered on the ethyl group of the molecule that could be subjected to modification to increase the affinity of emetine for the binding pocket (Figure 5B, labelled as the ‘contour edge’). Although based on the similarity with the binding site in humans it is unlikely that emetine can be structurally modified to not bind the mammalian system, as demonstrated in the case of dehydroemetine modifications can reduce its cytotoxicity. Although the mechanism for such reduced cytotoxicity mediated by pactamycin and emetine analogs is not known, it may be possible that these derived compounds selectively target tumor/parasite cells that are rapidly dividing, whereby protein synthesis is more sensitive to drug action in these cells. As in the case of antibiotics repurposed as antitumor agents, there is a clinical role for eukaryotic antibiotics that target systems with differential rates of translation provided usage is carefully directed. In malaria, eukaryotic antibiotics, such as emetine, could be used in combination with the slow-acting, but more specific apicoplast-targeting antibiotics (9).

This work demonstrates the power of contemporary cryo-EM for drug discovery. A drug, with a previously unknown binding site, can be visualized inside a macromolecular complex that is almost 10,000 times larger in molecular weight and at a level of detail comparable to that obtained by X-ray crystallography. By avoiding the need for crystallization one of the bottlenecks of solving a structure is bypassed. It allows structures to be solved from very small sample quantities, with sample heterogeneity improved through image processing. As such, cryo-EM is of particular use for solving the structures of macromolecules in their native state, isolated from pathogenic organisms where culturing large quantities is not possible.

In summary, our cryo-EM analyses reveal the first structure of a ribosome from a parasite at atomic resolution, along with detailed insights into the molecular basis of a known anti-protozoan translation inhibitor. Finally, it demonstrates that cryo-EM offers an attractive route towards the development of new compounds that target macromolecules by facilitating structure-activity relationships in otherwise intractable biological systems.

Materials and Methods

Parasite culture and ribosome purification

Wild type 3D7 strain of *P. falciparum* parasites were maintained in human erythrocytes (blood group O) at a hematocrit of 4% with 10% Albumax. Saponin lysed parasite pellets were incubated with lysis buffer (20 mM Hepes, pH 7.4, 250 mM KCl, 25 mM $Mg(CH_3COO)_2$, 0.15 % Triton, 5 mM 2-mecaptoethanol) at 4^{o}C for 1 hr. Ribosomes were purified by ultracentrifugation initially with a sucrose cushion (20 mM Hepes pH 7.4, 1.1 M sucrose, 40 mM KCH_3COO, 10 mM NH_4CH_3COO, 10 mM $Mg(CH_3COO)_2$ and 5 mM 2-mecaptoethanol) followed by a 10-40 % sucrose gradient separation step using the same buffer.

Electron microscopy

Aliquots of 3 µl of purified *Pf*80S at a concentration of ~160 nM (~0.5 mg/ml) were incubated for 30 s on glow-discharged holey carbon grids (Quantifoil R1.2/1.3), on which a home-made continuous carbon film (estimated to be ~30 Å thick) had previously been deposited. Grids were blotted for 2.5 s and flash frozen in liquid ethane using an FEI Vitrobot. For the empty *Pf*80S sample, grids were transferred to an FEI Titan Krios electron microscope that was operated at 300 kV. Images were recorded manually during two non-consecutive days on a back-thinned FEI Falcon II detector at a calibrated magnification of 135,922 (yielding a pixel size of 1.03 Å). Defocus values in the final data set ranged from 0.7-3.9 µm.

To prepare the *Pf*80S-emetine sample, purified *Pf*80S at 160 nM was incubated with a 1 mM solution of emetine in 20 mM Hepes pH7.4, 40 mM KCH_3COO, 10 mM NH_4CH_3COO, 10 mM $Mg(CH_3COO)_2$ and 5 mM 2-mecaptoethanol for 15 minutes at 25 °C prior to blotting and freezing as described above. *Pf*80S-emetine grids were transferred to an FEI Tecnai Polara electron microscope that was operated at 300 kV. Images were recorded manually during two non-consecutive days on a back-thinned FEI Falcon II detector at a calibrated magnification of 104,478 (yielding a pixel size of 1.34 Å). Defocus values in the final data set ranged from 0.8-3.8 µm.

During the data collection sessions of both samples, all images that showed signs of significant astigmatism or drift were discarded. An in-house built system was used to intercept the videos frames from the detector at a rate of 17 s^{-1} for the Krios and 16 s^{-1} for the Polara microscope.

Image processing

We used RELION (version 1.3-beta) for automated selection of 126,727 particles from 1,310

379 micrographs for the empty *Pf*80S sample; and 158,212 particles from 1,081 micrographs for
380 the *Pf*80S-emetine sample. Contrast transfer function parameters were estimated using
381 CTFFIND3 (40). All 2D and 3D classifications and refinements were performed using
382 RELION (41). To discard bad particles, we used a single round of reference-free 2D class
383 averaging with 100 classes for both data sets, and a single round of 3D classification with 4
384 classes for the *Pf*80S-emetine data set. The final refinement for the empty *Pf*80S and *Pf*80S-
385 emetine sample contained 72,293 and 105,247 particles, respectively. A 60 Å low-pass
386 filtered cryo-EM reconstruction of the yeast cytoplasmic 80S ribosome (EMDB-2275 (42))
387 was used as an initial model for the 3D refinement.
388
389 For the correction of beam-induced movements, we used statistical movie processing as
390 described previously (11), with running averages of five movie frames, and a standard
391 deviation of 1 pixel for the translational alignment. To further increase the accuracy of the
392 movement correction, we used the beta version of RELION-1.3 to fit linear tracks through the
393 optimal translations for all running averages, and included neighboring particles on the
394 micrograph in these fits. In addition, we employed a resolution and dose-dependent model
395 for the radiation damage, where each frame is weighted with a different B-factor as was
396 estimated from single-frame reconstructions. These procedures yielded maps with an overall
397 resolution of 3.4 Å for the empty *Pf*80S and 3.2 Å for *Pf*80S-emetine.
398
399 Reported resolutions are based on the gold-standard FSC=0.143 criterion (43), and were
400 corrected for the effects of a soft mask on the FSC curve using high-resolution noise
401 substitution (43). Soft masks were made by converting atomic models into density maps,
402 binarizing those, and adding cosine-shaped edges. Prior to visualization, all density maps
403 were corrected for the modulation transfer function (MTF) of the detector, and then
404 sharpened by applying a negative B-factor (Table 1) that was estimated using automated
405 procedures (44).
406
407 In order to locate emetine in the *Pf*80S-emetine reconstruction, we calculated a difference
408 map between the reconstructions of empty *Pf*80S and *Pf*80S-emetine. To this purpose, the
409 two MTF-corrected and B-factor sharpened maps were aligned with respect to each other
410 using the 'Fit in Map' functionality in UCSF Chimera (45), and the empty *Pf*80S map was re-
411 interpolated on the Cartesian grid of the *Pf*80S-emetine map prior to subtraction of the maps
412 in RELION. For visualization purposes, the resulting difference map was low-pass filtered at
413 4.5 Å and the threshold was set at 5 standard deviations as calculated within the area of the
414 *Pf*80S ribosome (Figure 4B). At this threshold, only one continuous U-shaped feature was
415 visible. The highest difference density inside this feature extended to 11 standard deviations

in the difference map.

Local resolution variations in all reconstructions were estimated using ResMap (46). Presumably due to unresolved structural heterogeneity the local resolution in the small ribosomal subunit was typically worse than in the large ribosomal subunit. Therefore, for the *Pf*80S-emetine structure, we performed two additional 'focussed' refinements, where we masked out the large or the small subunit at every iteration. This gave rise to two maps (Figure 1E) with improved density for either the small subunit (at an overall resolution of 3.3 Å) or the large ribosomal subunit (at an overall resolution of 3.1 Å), and these maps were used for the refinement of the atomic model as described below.

Model building and refinement

Ribosomal protein sequences from the 3D7 strain of *P. falciparum* were taken from *PlasmoDB* (47) and used as template sequences to obtain homology models generated from I-TASSER (48). Homology models were fitted into the reconstructed map of *Pf*80S using Chimera (45). Each protein was then subjected to a jiggle-fit and extensively rebuilt with sidechains placed into the map density using Coot v.0.8 (49). The sequences of the *Pf*80S rRNAs were obtained from *PlasmoDB* (47) and aligned using Clustal Omega (50) with the rRNA sequences extracted from the *Saccharomyces cerevisae (Sc)* 80S structure (PDB ID: 3U5B and 3U5D)(16). Conserved regions without insertions or deletions were extracted from the yeast structure, mutated and renumbered. These conserved sections were then connected by *de novo* building of RNA. The complete rRNA was then manually rebuilt in Coot to optimize the fit to density. Building was aided by secondary structure predictions downloaded from the Comparative RNA Website (51).

The model was refined using REFMAC v.5.8, which was modified for structures determined by cryo-EM (13, 52). The *Pf*80S atomic model was refined as separate 60S and 40S subunits in the two maps that were obtained for either subunit in the focused refinements of the cryo-EM reconstructions. Structure factors for the (Fourier-space) refinement in REFMAC were obtained by cutting out sections of the corresponding maps with a 3 Å radius from the center of each atom in the model, and structure factor phases were not altered during refinement.

Throughout refinement, reference and secondary structure restraints were applied to the ribosomal proteins using the *Sc*80S structure as a reference model (53). Base pair and parallelization restraints obtained using LIBG were also applied throughout refinement (13). The stereochemistry of the rRNA model was further improved using the ERRASER-PHENIX

453 pipeline (54). Ramachandran restraints were not applied during refinement to preserve
454 backbone dihedral angles for validation.
455
456 The R-factor and average overall Fourier shell correlation were monitored during refinement
457 (Table 1) and the final model was validated using MolProbity (55). For cross-validation
458 against over-fitting we randomly displaced the atoms of our final model (with an RMSD of 0.5
459 Å), and performed a fully restrained refinement against a map that was reconstructed from
460 only one of the two independent halves of the data that were used in our gold-standard FSC
461 procedure. We then calculated FSC curves between the resulting model and the half-map
462 against which it had been refined (FSC_{work}), as well as the FSC curve between that model
463 and the other half-map (FSC_{test}). The observation that the FSC_{work} and FSC_{test} curves nearly
464 overlap demonstrates the absence of overfitting of the model (Figure 1-figure supplement 1).
465
466 **Acknowledgements** We thank S. Ralph, B. Sleebs, D. Wilson, E. Zuccala, G. McFadden,
467 A. Cowman, J. Rayner, A. Ruecker, M. Delves, R. Sinden, S. Chen, C. Savva, J. Grimmett,
468 T. Darling, G. Murshudov and P. Emsley for helpful discussions and experimental
469 assistance; and V. Ramakrishnan for comments on the manuscript.
470

References

1. WHO. WHO (2012) World Malaria Report 2012. WHO. 2012.
2. Kremsner PG, Krishna S. Antimalarial combinations. Lancet. 2004 Jul 17-23;364(9430):285-94.
3. Grimberg BT, Mehlotra RK. Expanding the Antimalarial Drug Arsenal-Now, But How? Pharmaceuticals (Basel). 2011 May 1;4(5):681-712.
4. Miller LH, Baruch DI, Marsh K, Doumbo OK. The pathogenic basis of malaria. Nature. 2002 Feb 7;415(6872):673-9.
5. Jackson KE, Habib S, Frugier M, Hoen R, Khan S, Pham JS, et al. Protein translation in Plasmodium parasites. Trends Parasitol. 2011 Oct;27(10):467-76.
6. McFadden GI, Reith ME, Munholland J, Lang-Unnasch N. Plastid in human parasites. Nature. 1996 Jun 6;381(6582):482.
7. Waters AP, Syin C, McCutchan TF. Developmental regulation of stage-specific ribosome populations in Plasmodium. Nature. 1989 Nov 23;342(6248):438-40.
8. Goodman CD, Su V, McFadden GI. The effects of anti-bacterials on the malaria parasite Plasmodium falciparum. Mol Biochem Parasitol. 2007 Apr;152(2):181-91.
9. Dahl EL, Rosenthal PJ. Multiple antibiotics exert delayed effects against the Plasmodium falciparum apicoplast. Antimicrob Agents Chemother. 2007 Oct;51(10):3485-90.
10. Matthews H, Usman-Idris M, Khan F, Read M, Nirmalan N. Drug repositioning as a route to anti-malarial drug discovery: preliminary investigation of the in vitro anti-malarial efficacy of emetine dihydrochloride hydrate. Malaria Journal. 2013;12:359.
11. Bai XC, Fernandez IS, McMullan G, Scheres SH. Ribosome structures to near-atomic resolution from thirty thousand cryo-EM particles. Elife. 2013;2:e00461.
12. Allegretti M, Mills DJ, McMullan G, Kuhlbrandt W, Vonck J. Atomic model of the F420-reducing [NiFe] hydrogenase by electron cryo-microscopy using a direct electron detector. Elife. 2014;3:e01963.
13. Amunts A, Brown A, Bai XC, Llacer JL, Hussain T, Emsley P, et al. Structure of the yeast mitochondrial large ribosomal subunit. Science. 2014 Mar 28;343(6178):1485-9.
14. Rabl J, Leibundgut M, Ataide SF, Haag A, Ban N. Crystal structure of the eukaryotic 40S ribosomal subunit in complex with initiation factor 1. Science. 2011 Feb 11;331(6018):730-6.
15. Klinge S, Voigts-Hoffmann F, Leibundgut M, Arpagaus S, Ban N. Crystal structure of the eukaryotic 60S ribosomal subunit in complex with initiation factor 6. Science. 2011 Nov 18;334(6058):941-8.
16. Ben-Shem A, Garreau de Loubresse N, Melnikov S, Jenner L, Yusupova G, Yusupov M. The structure of the eukaryotic ribosome at 3.0 A resolution. Science. 2011 Dec 16;334(6062):1524-9.
17. Fernandez IS, Bai XC, Murshudov G, Scheres SH, Ramakrishnan V. Initiation of translation by cricket paralysis virus IRES requires its translocation in the ribosome. Cell. 2014 May 8;157(4):823-31.
18. Anger AM, Armache JP, Berninghausen O, Habeck M, Subklewe M, Wilson DN, et al. Structures of the human and Drosophila 80S ribosome. Nature. 2013 May 2;497(7447):80-5.
19. Hashem Y, des Georges A, Fu J, Buss SN, Jossinet F, Jobe A, et al. High-resolution cryo-electron microscopy structure of the Trypanosoma brucei ribosome. Nature. 2013 Feb 21;494(7437):385-9.

519 20. Sengupta J, Nilsson J, Gursky R, Spahn CM, Nissen P, Frank J. Identification of the
520 versatile scaffold protein RACK1 on the eukaryotic ribosome by cryo-EM. Nat Struct Mol
521 Biol. 2004 Oct;11(10):957-62.
522 21. Nilsson J, Sengupta J, Frank J, Nissen P. Regulation of eukaryotic translation by
523 the RACK1 protein: a platform for signalling molecules on the ribosome. EMBO Rep.
524 2004 Dec;5(12):1137-41.
525 22. Baum S, Bittins M, Frey S, Seedorf M. Asc1p, a WD40-domain containing adaptor
526 protein, is required for the interaction of the RNA-binding protein Scp160p with
527 polysomes. Biochem J. 2004 Jun 15;380(Pt 3):823-30.
528 23. Kossinova O, Malygin A, Krol A, Karpova G. The SBP2 protein central to
529 selenoprotein synthesis contacts the human ribosome at expansion segment 7L of the
530 28S rRNA. RNA. 2014 May 21.
531 24. Lobanov AV, Delgado C, Rahlfs S, Novoselov SV, Kryukov GV, Gromer S, et al. The
532 Plasmodium selenoproteome. Nucleic Acids Res. 2006;34(2):496-505.
533 25. Jenner L, Melnikov S, Garreau de Loubresse N, Ben-Shem A, Iskakova M,
534 Urzhumtsev A, et al. Crystal structure of the 80S yeast ribosome. Curr Opin Struct Biol.
535 2012 Dec;22(6):759-67.
536 26. Hashem Y, des Georges A, Dhote V, Langlois R, Liao HY, Grassucci RA, et al.
537 Structure of the mammalian ribosomal 43S preinitiation complex bound to the scanning
538 factor DHX29. Cell. 2013 May 23;153(5):1108-19.
539 27. Gonzalo P, Reboud JP. The puzzling lateral flexible stalk of the ribosome. Biol Cell.
540 2003 May-Jun;95(3-4):179-93.
541 28. Grollman AP. Inhibitors of protein biosynthesis. V. Effects of emetine on protein
542 and nucleic acid biosynthesis in HeLa cells. J Biol Chem. 1968 Aug 10;243(15):4089-94.
543 29. Dinos G, Wilson DN, Teraoka Y, Szaflarski W, Fucini P, Kalpaxis D, et al. Dissecting
544 the ribosomal inhibition mechanisms of edeine and pactamycin: the universally
545 conserved residues G693 and C795 regulate P-site RNA binding. Mol Cell. 2004 Jan
546 16;13(1):113-24.
547 30. Jimenez A, Carrasco L, Vazquez D. Enzymic and nonenzymic translocation by
548 yeast polysomes. Site of action of a number of inhibitors. Biochemistry. 1977 Oct
549 18;16(21):4727-30.
550 31. Goodwin LG, Hoare CA, Sharp TM. The chemotherapy of amoebiasis; introduction
551 and methods of biological assay. British journal of pharmacology and chemotherapy.
552 1948 Mar;3(1):44-8.
553 32. Dempsey JJ, Salem HH. An enzymatic electrocardiographic study on toxicity of
554 dehydroemetine. Br Heart J. 1966 Jul;28(4):505-11.
555 33. James RF. Malaria treated with emetine or metronidazole. Lancet. 1985 Aug
556 31;2(8453):498.
557 34. Madjar JJ, Nielsen-Smith K, Frahm M, Roufa DJ. Emetine resistance in chinese
558 hamster ovary cells is associated with an altered ribosomal protein S14 mRNA. Proc
559 Natl Acad Sci U S A. 1982 Feb;79(4):1003-7.
560 35. Brodersen DE, Clemons WM, Jr., Carter AP, Morgan-Warren RJ, Wimberly BT,
561 Ramakrishnan V. The structural basis for the action of the antibiotics tetracycline,
562 pactamycin, and hygromycin B on the 30S ribosomal subunit. Cell. 2000 Dec
563 22;103(7):1143-54.
564 36. Kühlbrandt W. The Resolution Revolution. Science. 2014;343:1443.
565 37. Otoguro K, Iwatsuki M, Ishiyama A, Namatame M, Nishihara-Tukashima A,
566 Shibahara S, et al. Promising lead compounds for novel antiprotozoals. J Antibiot
567 (Tokyo). 2010 Jul;63(7):381-4.

568 38. Lu W, Roongsawang N, Mahmud T. Biosynthetic studies and genetic engineering
569 of pactamycin analogs with improved selectivity toward malarial parasites. Chem Biol.
570 2011 Apr 22;18(4):425-31.
571 39. Chintana T, Sucharit P, Mahakittikun V, Siripanth C, Suphadtanaphongs W. In
572 vitro studies on the sensitivity of local Entamoeba histolytica to anti-amoebic drugs.
573 Southeast Asian J Trop Med Public Health. 1986 Dec;17(4):591-4.
574 40. Mindell JA, Grigorieff N. Accurate determination of local defocus and specimen
575 tilt in electron microscopy. J Struct Biol. 2003 Jun;142(3):334-47.
576 41. Scheres SH. RELION: implementation of a Bayesian approach to cryo-EM
577 structure determination. J Struct Biol. 2012 Dec;180(3):519-30.
578 42. Ben-Shem A, Jenner L, Yusupova G, Yusupov M. Crystal structure of the
579 eukaryotic ribosome. Science. 2010 Nov 26;330(6008):1203-9.
580 43. Chen S, McMullan G, Faruqi AR, Murshudov GN, Short JM, Scheres SH, et al. High-
581 resolution noise substitution to measure overfitting and validate resolution in 3D
582 structure determination by single particle electron cryomicroscopy. Ultramicroscopy.
583 2013 Dec;135:24-35.
584 44. Rosenthal PB, Henderson R. Optimal determination of particle orientation,
585 absolute hand, and contrast loss in single-particle electron cryomicroscopy. J Mol Biol.
586 2003 Oct 31;333(4):721-45.
587 45. Pettersen EF, Goddard TD, Huang CC, Couch GS, Greenblatt DM, Meng EC, et al.
588 UCSF Chimera--a visualization system for exploratory research and analysis. J Comput
589 Chem. 2004 Oct;25(13):1605-12.
590 46. Kucukelbir A, Sigworth FJ, Tagare HD. Quantifying the local resolution of cryo-
591 EM density maps. Nat Methods. 2014 Jan;11(1):63-5.
592 47. PlasmoDB: An integrative database of the Plasmodium falciparum genome. Tools
593 for accessing and analyzing finished and unfinished sequence data. The Plasmodium
594 Genome Database Collaborative. Nucleic Acids Res. 2001 Jan 1;29(1):66-9.
595 48. Roy A, Kucukural A, Zhang Y. I-TASSER: a unified platform for automated protein
596 structure and function prediction. Nat Protoc. 2010 Apr;5(4):725-38.
597 49. Emsley P, Lohkamp B, Scott WG, Cowtan K. Features and development of Coot.
598 Acta crystallographica Section D, Biological crystallography. 2010 Apr;66(Pt 4):486-
599 501.
600 50. Sievers F, Wilm A, Dineen D, Gibson TJ, Karplus K, Li W, et al. Fast, scalable
601 generation of high-quality protein multiple sequence alignments using Clustal Omega.
602 Mol Syst Biol. 2011;7:539.
603 51. Cannone JJ, Subramanian S, Schnare MN, Collett JR, D'Souza LM, Du Y, et al. The
604 comparative RNA web (CRW) site: an online database of comparative sequence and
605 structure information for ribosomal, intron, and other RNAs. BMC Bioinformatics.
606 2002;3:2.
607 52. Murshudov GN, Skubak P, Lebedev AA, Pannu NS, Steiner RA, Nicholls RA, et al.
608 REFMAC5 for the refinement of macromolecular crystal structures. Acta
609 crystallographica Section D, Biological crystallography. 2011 Apr;67(Pt 4):355-67.
610 53. Nicholls RA, Long F, Murshudov GN. Low-resolution refinement tools in
611 REFMAC5. Acta crystallographica Section D, Biological crystallography. 2012 Apr;68(Pt
612 4):404-17.
613 54. Chou FC, Sripakdeevong P, Dibrov SM, Hermann T, Das R. Correcting pervasive
614 errors in RNA crystallography through enumerative structure prediction. Nat Methods.
615 2013 Jan;10(1):74-6.

55. Chen VB, Arendall WB, 3rd, Headd JJ, Keedy DA, Immormino RM, Kapral GJ, et al. MolProbity: all-atom structure validation for macromolecular crystallography. Acta crystallographica Section D, Biological crystallography. 2010 Jan;66(Pt 1):12-21.
56. Ban N, Beckmann R, Cate JH, Dinman JD, Dragon F, Ellis SR, et al. A new system for naming ribosomal proteins. Curr Opin Struct Biol. 2014 Feb 10.

Figure legends

Figure 1. Cryo-EM data and processing. **(A)** Sucrose gradient purification of *Pf*80S ribosomes. **(B)** Representative electron micrograph showing *Pf*80S particles. (**C)** Fourier Shell Correlation (FSC) curves indicating the overall resolutions of unmasked (red), *Pf*40S masked (green) and *Pf*60S masked (blue) reconstructions of the *Pf*80S-emetine complex. (**D),** Representative density with built models of a β-strand with well-resolved side chains (left), an RNA segment with separated bases (middle), and a magnesium ion (green sphere) that is coordinated by RNA backbone phosphates. (**E**) Density maps colored according to local resolution for the unmasked *Pf*80S (left) and masked *Pf*40S and *Pf*60S subunits (right).

Figure 1-supplement figure 1. FSC curves between the final refined atomic model and the reconstructions from all particles (black); between the model refined in the reconstruction from only half of the particles and the reconstruction from that same half (FSC_{work}, red); and between that same model and the reconstruction from the other half of the particles (FSC_{test}, green), for *Pf*40S **(A)** and *Pf*60S **(B)**.

Figure 2. Structure of the *Pf*80S ribosome. Overview of *Pf*80S atomic model showing views facing **(A)** tRNA entry side and **(B)** tRNA exit side. rRNAs are shown in gray, proteins numbered according to (56). (**C-D**) *Pf*40S and *Pf*60S subunits are colored in yellow and blue respectively. Flexible regions are shown in red and at a resolution of 6 Å. *Pf*-specific expansion segments (ESs) relative to human ribosomes are labeled. Their numbering is as described for the human cytoplasmic ribosome (18).

Figure 2-supplement figure 1. Secondary structure of *Pf*18S rRNAs. *Pf*-specific ESs are highlighted in a labeled red box. Regions not built in the atomic model are colored in blue text. The secondary structure was modified from the CRW site (51).

Figure 2-supplement figure 2. Secondary structure of the 5' half of *Pf*28S rRNA. *Pf*-specific ESs are highlighted in a labeled red box. Regions not built in the atomic model are colored in blue text. The secondary structure was modified from the CRW site (51).

Figure 2-supplement figure 3. Secondary structure of the 3' half of *Pf*28S rRNA. *Pf*-specific ESs are highlighted in a labeled red box. Regions not built in the atomic model are colored in blue text. The secondary structure was modified from the CRW site (51).

Figure 3. Details of *Pf*-specific protein extensions and rRNA ESs near the (**A-B**) subunit interface **(C)** P stalk and **(D)** the L1 stalk. *Pf*-specific elements are shown in red.

Figure 4. Emetine binds to the E-site of the *Pf*40S subunit**. (A)** 2D chemical structure of emetine. (**B**) A 4.5 Å filtered difference map (red density) at 5 standard deviation overlaid with the *Pf*80S map filtered at 6 Å (blue and yellow for *Pf*60S and *Pf*40S respectively), showing the emetine density at the E-site of the *Pf*40S. The emetine binding site in (**C**) empty and (**D**) emetine-bound structures, with (**E**) density for emetine alone at 3.2 Å.

Figure 5. Molecular details of the emetine-ribosome interaction**. (A)** Overview of emetine at the binding interface formed by the 3 conserved rRNA helices and uS11. h23 is in green, h24 in cyan, h45 in blue, uS11 in pink and emetine in yellow. (**B**) 2D representation showing the interaction of emetine with binding residues. Substitution contour represents potential space for chemical modification of emetine. (**C**) Residues in physical contact with emetine. Hydrogen bond is indicated as dashes.

Figure 5-supplement figure 1. Comparison of the emetine binding residues between *Pf*80S and human ribosomes. Human and *Pf*-specific elements are colored in yellow and cyan respectively, with *Pf* numbering. Emetine is in purple.

Figure 6. Comparison with pactamycin. Superposition of emetine and pactamycin at the *Pf*40S emetine binding pocket. Emetine and pactamycin are shown in yellow and red respectively.

Table 1 Refinement and model statistics

Data Collection		***Pf*80S-emetine**	
	Particles	105,247	
	Pixel size (Å)	1.34	
	Defocus range (μm)	0.8-3.8	
	Voltage (kV)	300	
	Electron dose (e^{-} Å^{-2})	20	
		***Pf*60S**	***Pf*40S**
Model composition			
	Non-hydrogen atoms	124,509	68,858
	Protein residues	6,244	4,106
	RNA bases	3,460	1,682
	Ligands (Zn^{2+}/Mg^{2+}/emetine)	5/163/0	1/67/1
Refinement			
	Resolution used for refinement (Å)	3.1	3.3
	Map sharpening B-factor (Å^2)	-60.3	-79.9
	Average B factor (Å^2)	113.1	143.2
	Rfactor*	0.2294	0.257
	Fourier Shell Correlation†	0.86	0.854
Rms deviations			
	Bonds (Å)	0.006	0.007
	Angles (°)	1.20	1.29
Validation (proteins)			
	Molprobity score	2.45 (96th percentile)	2.73 (95th percentile)
	Clashscore, all atoms	3.65 (100th percentile)	4.23 (100th percentile)
	Good rotamers (%)	90.0	86.0
Ramachandran plot			
	Favored (%)	90.4	85.4
	Outliers (%)	2.4	4.2
Validation (RNA)			
	Correct sugar puckers (%)	97.3	97.5
	Good backbone conformations (%)	71.1	70.0

*Rfactor = $\Sigma||F_{obs}|-||F_{calc}| / \Sigma|F_{obs}|$

† $FSC_{overall} = \Sigma(N_{shell}\ FSC_{shell}) / \Sigma(N_{shell})$, where FSC_{shell} is the FSC in a given shell, N_{shell} is the number of 'structure factors' in the shell. $FSC_{shell} = \Sigma(F_{model}\ F_{EM})/(\sqrt{(\Sigma(|F|^2_{model}))}\ \sqrt{(\Sigma(F^2_{EM}))}$

691 **Table 2 Ribosomal proteins of the *Pf*40S subunit.**

Protein names	Uniprot ID	PlasmoDB ID	Chain ID	Built residues	Extensions compared to human	Total number of residues
eS1	RS3A_PLAF7	PF3D7_0322900	B	24-233	245-262	262
uS2	RSSA_PLAF7	PF3D7_1026800	C	10-204	-	263
uS3	Q8IKH8_PLAF7	PF3D7_1465900	D	4-39; 65-78; 97-193; 207-216	-	221
uS4	Q8I3R0_PLAF7	PF3D7_0520000	E	2-186	-	189
eS4	Q8IIU8_PLAF7	PF3D7_1105400	F	2-258	-	261
uS5	Q8IL02_PLAF7	PF3D7_1447000	G	39-262	-	272
eS6	Q8IDR9_PLAF7	PF3D7_1342000	H	1-160; 170-213	249-306	306
uS7	Q8IBN5_PLAF7	PF3D7_0721600	I	7-118; 128-195	-	195
eS7	Q8IET7_PLAF7	PF3D7_1302800	J	3-190	-	194
uS8	O77395_PLAF7	PF3D7_0316800	K	2-130	-	130
eS8	Q8IM10_PLAF7	PF3D7_1408600	L	5-120; 161-213; 216-218	154-163	218
uS9	Q8IAX5_PLAF7	PF3D7_0813900	M	6-143	-	144
uS10	Q8IK02_PLAF7	PF3D7_1003500	N	21-118	-	118
eS10	Q8IBQ5_PLAF7	PF3D7_0719700	O	11-89	-	137
uS11	Q8I3U6_PLAF7	PF3D7_0516200	P	25-151	-	151
uS12	O97248_PLAF7	PF3D7_0306900	Q	2-145	-	145
eS12	RS12_PLAF7	PF3D7_0307100	R	22-78; 85-100; 111-135	10-16	141
uS13	Q8IIA2_PLAF7	PF3D7_1126200	S	12-139	-	156
uS14	C0H4K8_PLAF7	PF3D7_0705700	T	7-54	-	54
uS15	Q8IDB0_PLAF7	PF3D7_1358800	U	3-151	-	151
uS17	O77381_PLAF7	PF3D7_0317600	V	6-25; 36-161	-	161
eS17	Q8I502_PLAF7	PF3D7_1242700	W	3-83; 97-110	-	137
uS19	C0H5C2_PLAF7	PF3D7_1317800	X	21-95; 103-123	-	145
eS19	Q8IFP2_PLAF7	PF3D7_0422400	Y	15-168	1-19	170
eS21	Q8IHS5_PLAF7	PF3D7_1144000	Z	11-82	-	82
eS24	Q8I3R6_PLAF7	PF3D7_0519400	1	3-122	-	133
eS25	Q8ILN8_PLAF7	PF3D7_1421200	2	35-42; 58-84; 97-102	-	105
eS26	O96258_PLAF7	PF3D7_0217800	3	2-96	-	107
eS27	Q8IEN2_PLAF7	PF3D7_1308300	4	7-82	-	82
eS28	Q8IKL9_PLAF7	PF3D7_1461300	5	2-29; 37-66	-	67
eS30	RS30_PLAF7	PF3D7_0219200	6	6-48	-	58
eS31	Q8IM64_PLAF7	PF3D7_1402500	-	Not built	-	149

692
693

Table 3 Ribosomal proteins of the *Pf*60S subunit.

Protein names	Uniprot ID	PlasmoDB ID	Chain ID	Built residues	Extensions compared to human	Total number of residues
uL2	Q8I3T9_PLAF7	PF3D7_0516900	D	2-248	-	260
uL3	Q8IJC6_PLAF7	PF3D7_1027800	E	2-381	-	386
uL4	Q8I431_PLAF7	PF3D7_0507100	F	6-395	373-411	411
uL5	Q8IBQ6_PLAF7	PF3D7_0719600	G	8-51; 64-85; 92-106; 124-166	-	173
uL6	Q8IE85_PLAF7	PF3D7_1323100	H	2-186	-	190
eL6	Q8IDV1_PLAF7	PF3D7_1338200	I	9-151; 158-221	110-118; 139-143; 174-182	221
eL8	Q8ILL2_PLAF7	PF3D7_1424400	J	40-46; 54-131; 147-283	11-24;279-283	283
uL13	Q8IJZ7_PLAF7	PF3D7_1004000	K	1-201	-	202
eL13	Q8IAX6_PLAF7	PF3D7_0814000	L	2-212	134-141; 168-174	215
uL14	Q8IE09_PLAF7	PF3D7_1331800	M	8-139	-	139
eL14	Q8ILE8_PLAF7	PF3D7_1431700	N	5-150	1-18	165
uL15	C6KT23_PLAF7	PF3D7_0618300	O	2-148	-	148
eL15	C0H4A6_PLAF7	PF3D7_0415900	P	2-205	-	205
uL16	Q8ILV2_PLAF7	PF3D7_1414300	Q	2-101; 118-206	-	219
uL18	Q8ILL3_PLAF7	PF3D7_1424100	R	5-126; 141-185; 189-250; 271-293	-	294
eL18	C0H5G3_PLAF7	PF3D7_1341200	U	5-184	-	184
eL19	C6KSY6_PLAF7	PF3D7_0614500	T	2-182	-	182
eL20	Q8IDS6_PLAF7	PF3D7_1341200	S	2-187	-	184
eL21	Q8ILK3_PLAF7	PF3D7_1426000	V	4-158	-	161
uL22	Q8IDI5_PLAF7	PF3D7_1351400	W	4-154; 197-215	-	203
eL22	Q8IB51_PLAF7	PF3D7_0821700	X	40-136	4-18; 34-38	139
uL23	Q8IE82_PLAF7	PF3D7_1323400	Y	88-188	13-34; 57-67	190
uL24	O77364_PLAF7	PF3D7_0312800	Z	2-122	-	126
eL24	Q8IEM3_PLAF7	PF3D7_1309100	0	8-69	-	162
eL27	Q8IKM5_PLAF7	PF3D7_1460700	1	2-126;132-146	-	146
eL28	Q8IHU0_PLAF7	PF3D7_1142500	2	2-69; 77-82; 86-98; 103-119	-	127
uL29	Q8IIB4_PLAF7	PF3D7_1124900	3	3-121	-	124
eL29	C6S3J6_PLAF7	PF3D7_1460300	4	2-67	-	67
uL30	O97250_PLAF7	PF3D7_0307200	5	35-257	-	257
eL30	Q8IJK8_PLAF7	PF3D7_1019400	6	8-105	-	108
eL31	Q8I463_PLAF7	PF3D7_0503800	7	15-88; 95-116	-	120
eL32	Q8I3B0_PLAF7	PF3D7_0903900	8	2-126	-	131
eL33	Q8IHT9_PLAF7	PF3D7_1142600	9	35-137	1-35	140
eL34	Q8IBY4_PLAF7	PF3D7_0710600	a	2-107	-	150
eL36	Q8I713_PLAF7	PF3D7_1109900	b	2-27; 38-106	5-10	112
eL37	C0H4L5_PLAF7	PF3D7_0706400	c	2-90	-	92
eL38	Q8II62_PLAF7	PF3D7_1130100	d	2-31; 36-77	-	87
eL39	C0H4H3_PLAF7	PF3D7_0611700	e	2-30;38-51	-	51
eL40	Q8ID50_PLAF7	PF3D7_1365900	f	1-51	-	52
eL41	C6S3G4_PLAF7	PF3D7_1144300	g	3-39	1-14	39
eL43	RL37A_PLAF7	PF3D7_0210100.1	h	2-86	-	96
eL44	RL44_PLAF7	PF3D7_0304400	i	2-96	-	104

Table 4: Comparison of ESs in *Pf*80S and human cytoplasmic ribosomes.

rRNA	ES	Helix	Comparison between *Pf*80S and human ribosomes
18S	ES2S		Shorter loop in *Pf*80S
	ES3S	A	Conserved
		B	Truncated in *Pf*80S
	ES13S		Conserved
	ES6S	A	Expanded in *Pf*80S
		B	Truncated in *Pf*80S
		C	Conserved
		D	Expanded in *Pf*80S
		E	Conserved
	ES7S		Expanded in *Pf*80S
	ES14S		Conserved
	ES9S		Expanded in *Pf*80S
	ES10S		Expanded in *Pf*80S
	ES12S		Helix truncated in *Pf*80S
28S	ES3L		Conserved
	ES4L		Conserved
	ES5L		Conserved
	ES7L	A	Truncated in *Pf*80S
		B	Truncated. Loop in *Pf*80S forms a novel interaction with eL14
		B1	*Pf*-specific ES
		C	Present
		D-H	Absent from *Pf*80S
	ES8L	H28	Expanded in *Pf*80S
	ES9L	A	Absent in *Pf*80S
		H30	Conserved
		H31	Conserved
	ES10L		Absent in *Pf*80S
	ES12L		Expanded in *Pf*80S
	ES15L	A	Truncated in *Pf*80S
	ES19L		Truncated in *Pf*80S
	ES20L	A	Absent in *Pf*80S
		B	Conserved in *Pf*80S
	ES26L		Expanded in *Pf*80S
	ES27L	A-C	Not present in Pf80S model, predicted divergence between *Pf* and human cytoplasmic ribosomes
	ES30L		Absent in *Pf*80S
	ES31L	A	Conserved
		B	Expanded in *Pf*80S
		C	Conserved
	ES34L		*Pf*-specific ES
	ES36L		*Pf*-specific ES
	ES39L	A	Conserved; preceding loop in *Pf*80S forms a short helix (3 base pairs) with the 5' end of the 5.8S rRNA
		B	Conserved
	ES41L		Conserved

Additional information

Competing interests

The authors declare no competing financial interests. Correspondence and requests for materials should be addressed to S.H.W.S. (scheres@mrc-lmb.cam.ac.uk) or J.B. (jake.baum@imperial.ac.uk).

Funding

Funder	Grant reference number	Author
Victorian State Government Operational Infrastructure Support and Australian Government NHMRC IRIISS	N/A	
National Health and Medical Research Council of Australia	APP1024678 Project Grant	Jake Baum Wilson Wong
National Health and Medical Research Council of Australia	APP1053801 Peter Doherty fellowship	Wilson Wong
Human Frontier Science Program	RGY0071/2011 Young Investigator Program Grant	Jake Baum
UK Medical Research Council	MC_UP_A025_1013	Sjors Scheres
UK Medical Research Council	MC_U105184332	Alan Brown Israel S. Fernandez
OzEMalaR	Travel Grant	Wilson Wong
EU FP7 Marie Curie	N/A	Xiaochen Bai
Wellcome Trust	WT096570	Alan Brown Israel S. Fernandez
Australian Research Council	FT100100112 Future fellowship	Jake Baum
Wellcome Trust	100993/Z/13/Z New Investigator Award	Jake Baum

The funders had no role in study design, data collection and interpretation, or the decision to submit the work for publication.

Author contributions

WW, Conception and design, Acquisition of data, Analysis and interpretation of data, Drafting or revising the article, X-CB, Acquisition of data, Analysis and interpretation of data, A.B. Analysis and interpretation of data, Drafting or revising the article; ISF, Ribosome purification, EH, Contributed unpublished essential data or reagents, MC, YHT, prepared parasite lysates for ribosome purification, J.B. Conception and design, Analysis and interpretation of data, Drafting or revising the article, SHWS, Conception and design, Analysis and interpretation of data, Drafting or revising the article.

732 **Additional files**

733 **The following datasets were created:**

734

Author(s)	Year	Dataset title	Dataset ID and/or URL	Database, license and accessibility information
Wong W, Bai X-C, Brown A, Fernandez IS, Hanssen E, Condron C, Tan YH, Baum J, Scheres SHW	2014	*Plasmodium falciparum* 80S ribosome bound to the anti-protozoan drug emetine	EMD-2660	Publicly available at the Electron Microscopy Data Bank (http://www.ebi.ac.uk/pdbe/emdb/).
Wong W, Bai X-C, Brown A, Fernandez IS, Hanssen E, Condron C, Tan YH, Baum J, Scheres SHW	2014	*Plasmodium falciparum* 80S ribosome	EMD-2661	Publicly available at the Electron Microscopy Data Bank (http://www.ebi.ac.uk/pdbe/emdb/).
Wong W, Bai X-C, Brown A, Fernandez IS, Hanssen E, Condron C, Tan YH, Baum J, Scheres SHW	2014	Cryo-EM structure of the *Plasmodium falciparum* 80S ribosome bound to the anti-protozoan drug emetine; large subunit	3J79	Publicly available at the RCSB Protein Data Bank (http://www.rcsb.org/pdb/).
Wong W, Bai X-C, Brown A,	2014	Cryo-EM structure of the	3J7A	Publicly available at the RCSB Protein Data Bank (http://www.rcsb.org/

Fernandez IS, Hanssen E, Condron C, Tan YH, Baum J, Scheres SHW		*Plasmodium falciparum* 80S ribosome bound to the anti-protozoan drug emetine; small subunit		pdb/).

735

736 The following previously published datasets were used:

737

Author(s)	**Year**	**Dataset title**	**Dataset ID and/or URL**	**Database, license and accessibility information**
Bai X-C, Fernadez IS, McMullan G, Scheres SHW	2013	Ribosome structures at near-atomic resolution from thirty thousand cryo-EM particles	EMDB-2275	Publicly available at the Electron Microscopy Data Bank (http://www.ebi.ac.uk/pdbe/emdb/).
Ben-Shem A, Garreau de Loubresse N, Meinikov S, Jenner L, Yusupov G, Yusupov M	2011	The structure of the eukaryotic ribosome at 3.0 Å resolution	3U5B	Publicly available at the RCSB Protein Data Bank (http://www.rcsb.org/pdb/).
Ben-Shem A, Garreau de Loubresse N, Meinikov S, Jenner L,	2011	The structure of the eukaryotic ribosome at 3.0 Å	3U5C	Publicly available at the RCSB Protein Data Bank (http://www.rcsb.org/pdb/).

Yusupov G, Yusupov M		resolution		
Ben-Shem A, Garreau de Loubresse N, Meinikov S, Jenner L, Yusupov G, Yusupov M	2011	The structure of the eukaryotic ribosome at 3.0 Å resolution	3U5D	Publicly available at the RCSB Protein Data Bank (http://www.rcsb.org/pdb/).
Ben-Shem A, Garreau de Loubresse N, Meinikov S, Jenner L, Yusupov G, Yusupov M	2011	The structure of the eukaryotic ribosome at 3.0 Å resolution	3U5E	Publicly available at the RCSB Protein Data Bank (http://www.rcsb.org/pdb/).
Anger AM, Armache JP, Berninghausen O, Habeck M, Subklewe M, Wilson DN, Beckmann R	2013	Structure of the human 40S ribosomal proteins	3J3A	Publicly available at the RCSB Protein Data Bank (http://www.rcsb.org/pdb/).
Anger AM, Armache JP, Berninghausen O, Habeck M, Subklewe M, Wilson DN, Beckmann R	2013	Structure of the human 60S ribosomal proteins	3J3B	Publicly available at the RCSB Protein Data Bank (http://www.rcsb.org/pdb/).
Anger AM, Armache JP, Berninghausen	2013	Structure of the *H. sapiens* 40S rRNA and	3J3D	Publicly available at the RCSB Protein Data Bank (http://www.rcsb.org/pdb/).

O, Habeck M, Subklewe M, Wilson DN, Beckmann R		E-tRNA		
Anger AM, Armache JP, Berninghausen O, Habeck M, Subklewe M, Wilson DN, Beckmann R	2013	Structure of the *H. sapiens* 60S rRNA	3J3F	Publicly available at the RCSB Protein Data Bank (http://www.rcsb.org/pdb/).

738
739
740
741
742
743
744

Figure 1

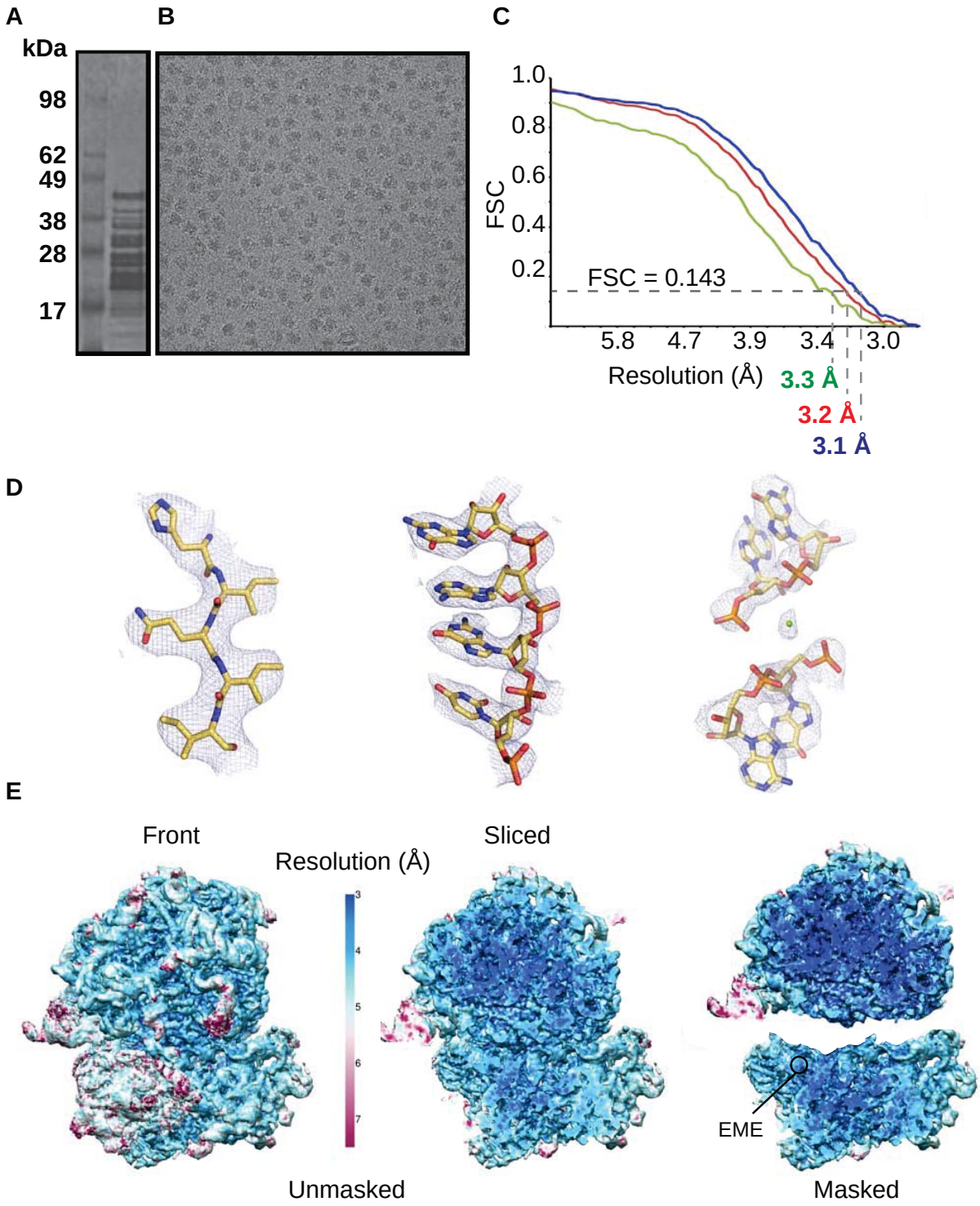
A
B
C
kDa
98
62
49
38
28
17
1.0
0.8
0.6
0.4
0.2
FSC
FSC = 0.143
5.8
4.7
3.9
3.4
3.0
Resolution (Å)
3.3 Å
3.2 Å
3.1 Å
D
E
Front
Sliced
Resolution (Å)
3
4
5
6
7
EME
Unmasked
Masked

Figure 2

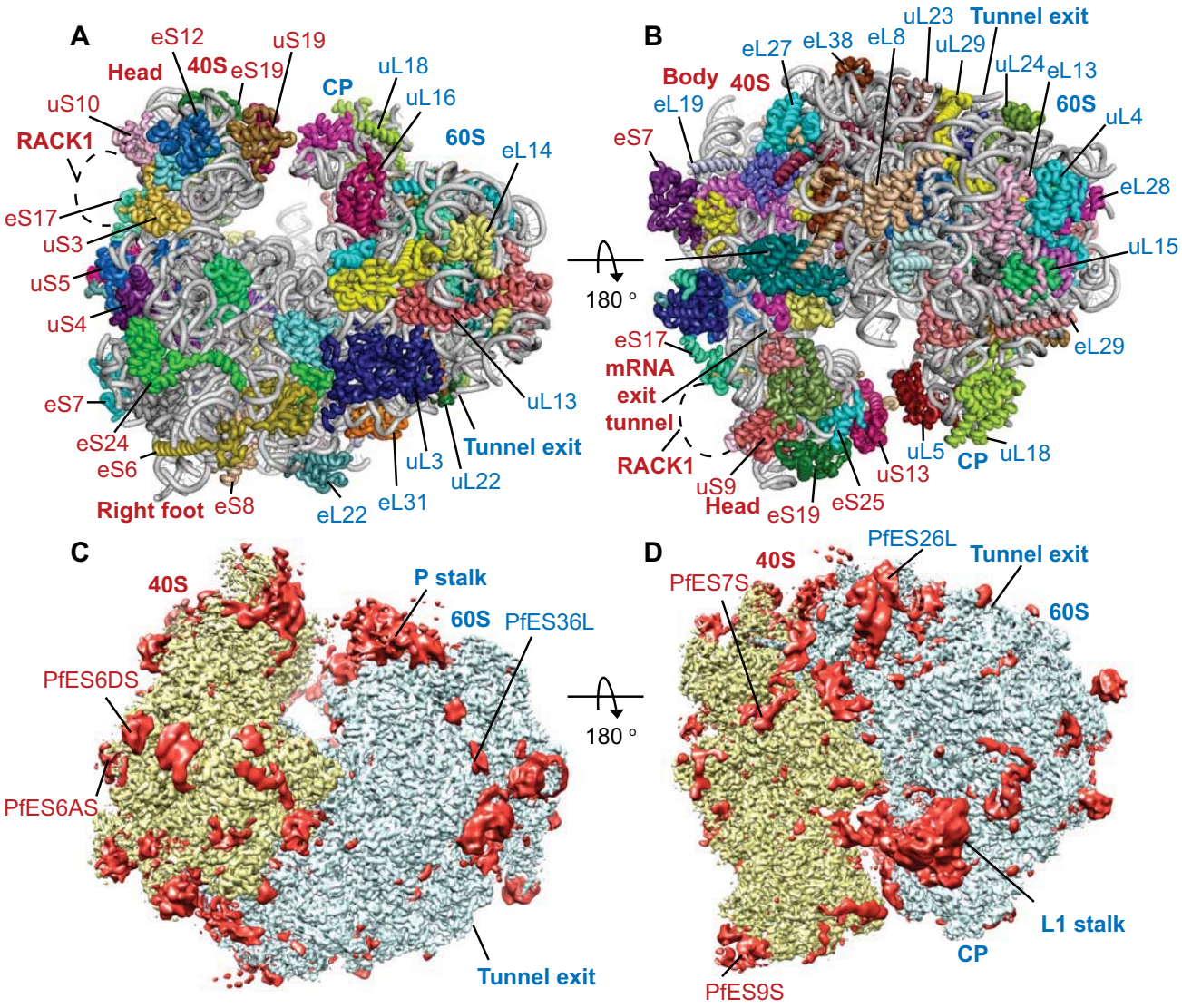
A
eS12
uS19
Head
40S
eS19
CP
uL18
uS10
uL16
RACK1
60S
eL14
eS17
uS3
uS5
uS4
eS7
uL13
eS24
Tunnel exit
eS6
uL3
uL22
Right foot
eS8
eL22
eL31
B
uL23
Tunnel exit
eL27
eL38
eL8
uL29
uL24
eL13
Body
40S
60S
eL19
uL4
eS7
eL28
uL15
180 °
eS17
eL29
mRNA
exit
tunnel
RACK1
uL5
CP
uL18
uS9
uS13
Head
eS19
eS25
C
40S
P stalk
60S
PfES36L
PfES6DS
PfES6AS
180 °
Tunnel exit
D
PfES26L
40S
Tunnel exit
PfES7S
60S
L1 stalk
CP
PfES9S

Figure 3

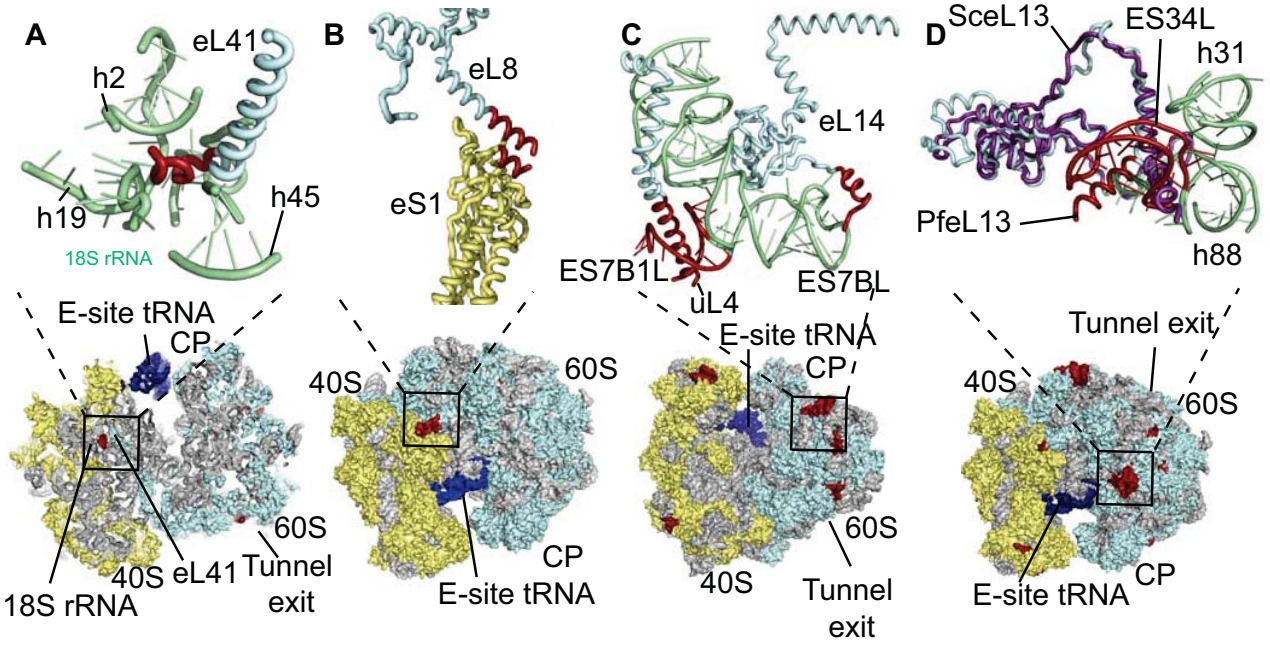
A
eL41
h2
h19
h45
18S rRNA
E-site tRNA
CP
60S
40S
eL41
Tunnel exit
18S rRNA
B
eL8
eS1
40S
60S
CP
E-site tRNA
C
eL14
ES7B1L
uL4
ES7BL
E-site tRNA
CP
60S
40S
Tunnel exit
D
SceL13
ES34L
h31
PfeL13
h88
Tunnel exit
40S
60S
CP
E-site tRNA

Figure 4

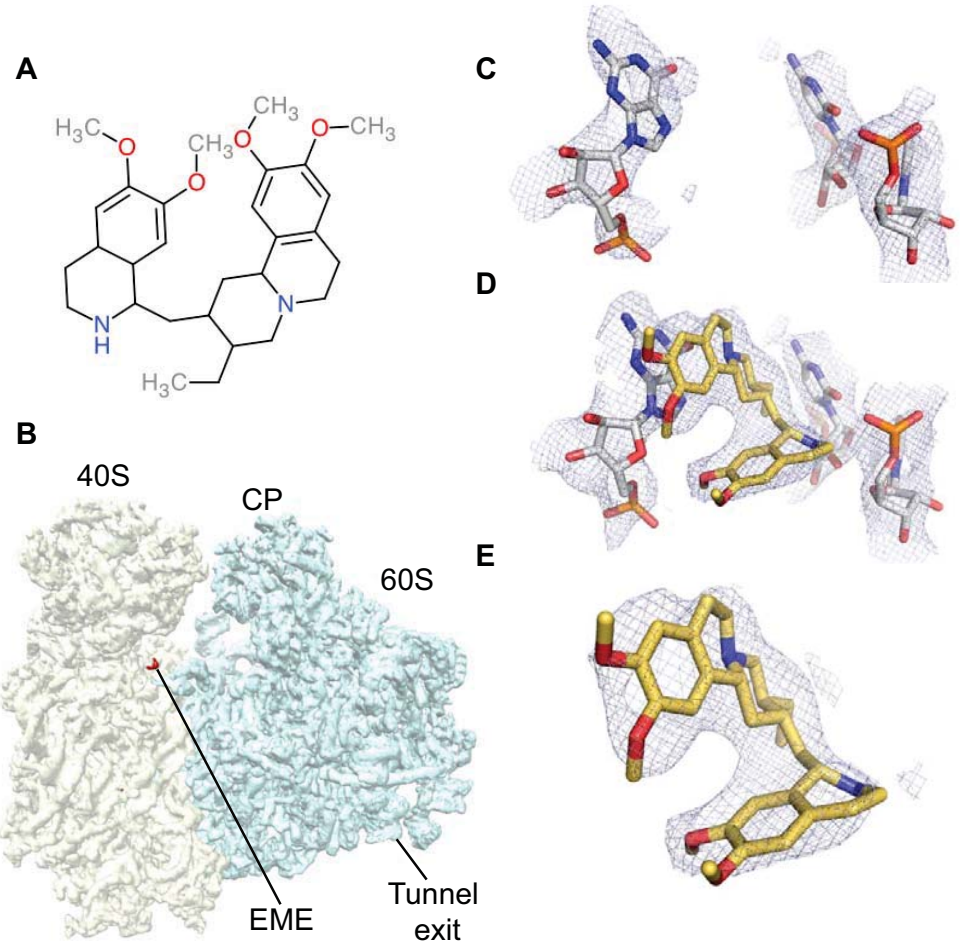

Figure 5

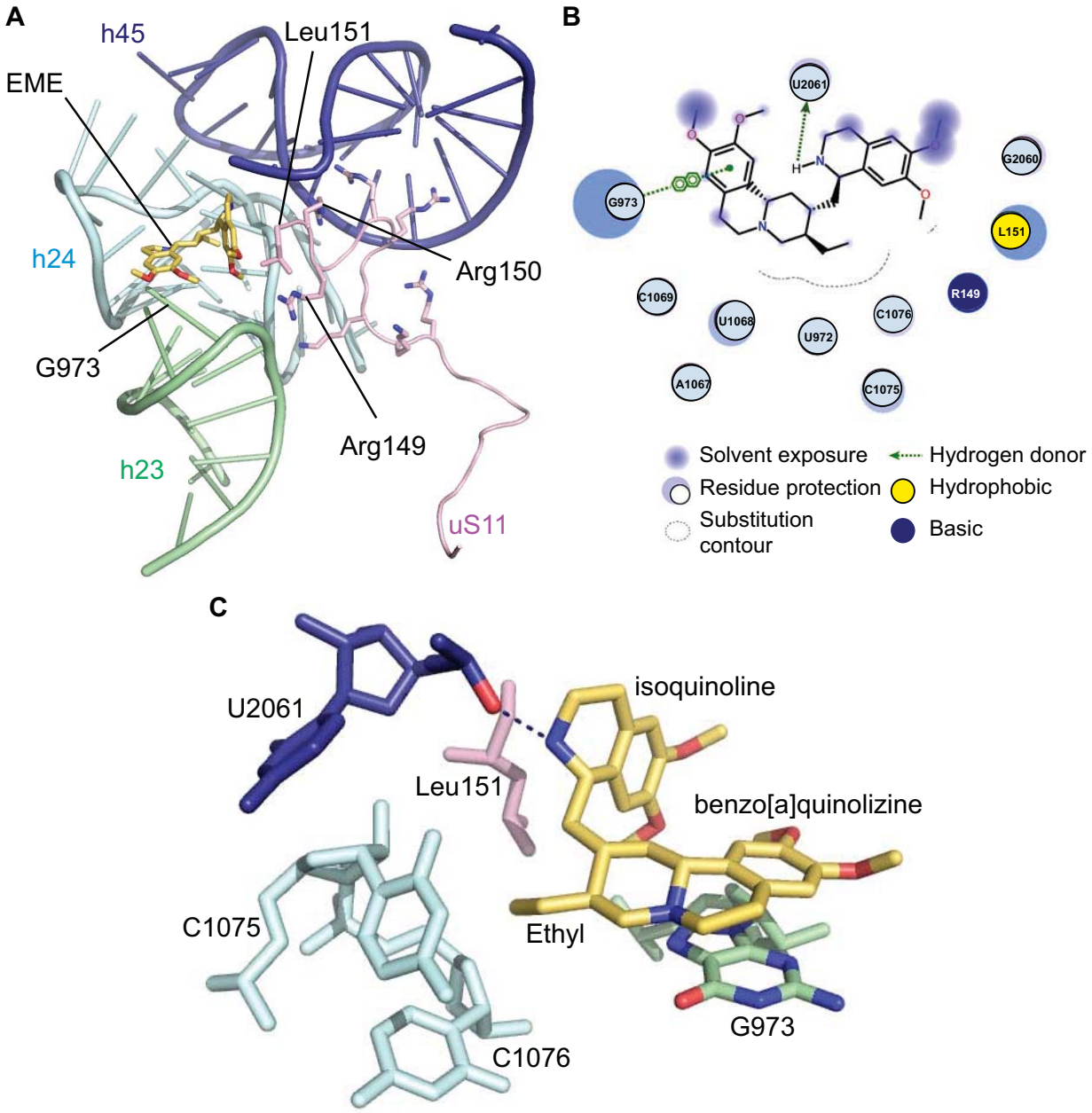
A
h45
Leu151
EME
h24
Arg150
G973
Arg149
h23
uS11
B
U2061
G2060
G973
L151
C1069
R149
U1068
C1076
U972
A1067
C1075
Solvent exposure
Residue protection
Substitution contour
Hydrogen donor
Hydrophobic
Basic
C
U2061
isoquinoline
Leu151
benzo[a]quinolizine
C1075
Ethyl
G973
C1076

Figure 6